Development of electrochemical cells for spatially resolved analysis using a multi-technique approach: from conventional experiments to X-ray nanoprobe beamlines

Rafael A. Vicente[a,b], Swathi P. Raju[a,b], Heloisa V. N. Gomes[a,b], Itamar T. Neckel[c]*, Hélio C. N. Tolentino[c], Pablo S. Fernández[a,b]*

[a] MsC, R.A. Vicente, Ms. S. P. Raju, Ms. H. V. N. Gomes, Dr. P. S. Fernández
Campinas Electrochemistry Group
Physical Chemistry Department
State University of Campinas, Department
R. Josué de Castro, s/n, Campinas, Brazil
pablosf@unicamp.br

[b] MsC, R.A. Vicente, Ms. S. P. Raju, Ms. H. V. N. Gomes, Dr. P. S. Fernández
Center for Innovation on New Energies (CINE)
R. Michel Debrun, s/n, Prédio Amarelo, Campinas, Brazil

[c] Dr. H. C. N. Tolentino, Dr. I. T. Neckel
Brazilian Synchrotron Light Laboratory (LNLS)
Brazilian Center for Research in Energy and Materials (CNPEM)
R. Giuseppe Máximo Scolfaro, 10000 - Bosque das Palmeiras, Campinas, Brazil
Itamar.neckel@lnls.br

Abstract: Real (electro-)catalysts are often heterogeneous, and their activity and selectivity depend on the properties of specific active sites. Therefore, unveiling the so-called structure-activity relationship is essential for a rational search for better materials and, consequently, for the development of the field of (electro-)catalysts. Thus, spatially resolved techniques are powerful tools as they allow us to characterize and/or measure the activity and selectivity of different regions of heterogeneous catalysts. To take full advantage of that, we have developed spectroelectrochemical cells (SEC) to perform spatially resolved analysis using X-ray nanoprobe synchrotron beamlines, and conventional pieces of equipment. Here, we describe the techniques available at the Carnaúba beamline at Sirius-LNLS storage ring, then we show how our SECs enable obtaining X-ray (XRF, XRD, XAS, etc.) and vibrational spectroscopy (FTIR and Raman) contrast images. Through some proof-of-concept experiments, we demonstrate how using a multi-technique approach could render a complete and detailed analysis of an (electro-)catalyst overall performance.

Introduction

Electrochemistry is considered as one of the most important subjects in the field of new energies,[1] contributing to the development of fuel cells for energy conversion,[2,3] and electrolyzers for hydrogen production,[4,5] among several other applications. Many of these (electro-)catalytic devices use heterogeneous structures, for instance, the catalysts, which span from the micro to the nanoscale. Thus, one of the most active research areas is related to the development (or improvement) of more efficient and durable catalysts.[6–9] To succeed in this task, it is mandatory a deep understanding of the relation between the catalyst composition and structure with its performance (activity, selectivity and durability), i.e., the so-called structure-activity relationship. Unfortunately, except for some model systems,[10–13] it is tricky to succeed in this task due to the multiple factors playing a relevant and simultaneous role in (electro-)catalytic processes.[14]

It is worth pointing out that there is an intrinsic complexity introduced by the word “structure” in this field: depending on the system/material of interest, it can refer to the shape, and/or size, and/or facet crystallographic orientation, and/or crystallographic structure, etc. For instance, in electrochemistry, many of these structural properties can play an important role on the material activity. Shape control in nanoparticulated catalysts is a deciding factor for its activity, and it is a common strategy to synthesize shape-controlled crystals to control particle facet distribution and size to improve the catalytic activity[15–18] or to drive the selectivity of the reaction to the desired product.[17,19] The exposed crystalline facets orientation also immensely affects the material activity/selectivity since different facets have different surface energy and, consequently, different adsorption energies.[20–22] In addition, size by itself is a deciding factor for several nanostructures since it defines nanoparticle (NP) activity.[12,13,23–26] These examples above summarize how the structure plays a major role in determining the activity, selectivity and stability of (electro-)catalytic materials.

The catalysts employed in (electro-)catalytic systems can be very diverse in terms of particle/grain sizes, ranging from the micro down to the nanoscale. Microstructures resemble bulk materials, being easier to analyze using model systems, such as single crystals.[27,28] However, the heterogeneity in these materials play a major role in their reactivity/activity since grains with different crystallographic orientation and grain boundaries can behave considerably differently.[29,30] Nanomaterials, on the other hand, permit maximizing the surface/area ratio, making them a usual choice for electrode materials employed in electrocatalytic systems[31,32] or in the field of heterogeneous catalysis.[33,34] Despite these advantages, correlating morphology and activity at the nanoscale is much more challenging, but still a very relevant topic.[10,35]

Not only the structure of the catalyst defines the (electro-)catalyst performance, but also the interactions between their components. The interactions between particles in a nanoparticulated catalyst,[36] and also the interactions with the substrate[23] (materials in real applications are even much more complex),

affect the (electro-)catalytic performance of the electrode. Moreover, the distribution of the active material on the support, i.e., the degree of agglomeration (which also impacts the behavior of the material[37,38]), depends on the interactions between the materials composing the electrode and/or on the preparation method. For example, the products generated in a region with many agglomerated NPs (which may or may not be in contact, but are close enough to perceive the existence of the other NPs) have a bigger chance of finding another NP and eventually reacting further, forming new products which are not detectable if the same reaction occurs on isolated NPs.[39] Besides, the isolated NP will interact with the reactants/intermediates/products and the support, while the agglomerated will interact with all of the above and also other NPs, which can induce different intrinsic activity. Therefore, analyzing the structure-activity relation with the spatial resolution is essential to try to isolate some of these effects.

Linking activity/selectivity to the heterogeneous structure/composition of (electro-)catalysts would be straightforward if we had a technique with the capability to fully characterize a region of a catalyst (could be also an isolated NP) and measure at the same time the activity of the same region (or of the same NP). However, despite the current arsenal of available characterization techniques in the field of (electro-)catalysts,[40–46] each of them with their strengths and weaknesses, there is not a technique able to generate this kind of data, especially with a spatially resolved methodology. Therefore, this problem must be tackled by using a multi-technique approach.

In this context, the development of fourth-generation synchrotrons and nanoprobe beamlines provide unique opportunities for the progress of several areas of science and technology, including (electro-)catalysis and electrochemistry in general, which are the main fields of interest here. These new facilities offer techniques with improved spatial resolution which can be promptly coupled together, or with other techniques employing conventional pieces of equipment.

Herein, we will focus on the possibilities offered by the recently launched CARNAÚBA (Coherent X-ray Nanoprobe Beamline) at Sirius Brazilian synchrotron facility.[47] We will briefly describe the techniques available at the beamline and how we envision each of them could be used in the field of (electro-)catalysis. Then, we will present the instrumentation (electrochemical cells) that we have designed to be used in this facility and some results obtained at the beamline with the aim of more clearly illustrating the capabilities of the setup. Lastly, we will show a versatile device that permits to correlate the information obtained using X-ray-based techniques performed at the beamline with vibrational spectroscopic analysis. We hope our developments will contribute to the challenging task of correlating activity with structure in (electro-)catalysis, impacting the progress of new materials in several fields.

Results and Discussion

CHARACTERIZATION TECHNIQUES AVAILABLE AT THE CARNAÚBA BEAMLINE.

Carnaúba is an X-ray nanoprobe beamline dedicated to multi-analytical analysis and imaging, working in an energy range from 2.05 to 15 keV.[48] Several X-ray nanoprobes have been developed during the past decade, covering from soft to hard X-ray energies.[49] In this beamline, the sample is raster-scanned, providing access to bidimensional maps or tomographic analysis. At Carnaúba, the available techniques are X-ray Absorption Spectroscopy (XAS), X-ray Fluorescence (XRF), X-ray Excited Optical Luminescence (XEOL), X-ray Diffraction (XRD), Ptychography and Bragg Coherent Diffraction Imaging (BCDI)[50] with nanometric spatial resolution. We guide the reader to more specific literature for more in-depth technical information about the beamline.[47]

The beamline was designed with two end-stations for different purposes:[47] Sapoti, which will work in a complete vacuum with a cryogenic support, and Tarumã, which works in-air with more space for diverse and flexible experimental setups and coupling of ancillary instruments and detectors (figure 1). Due to Tarumã's versatility, a wide variety of *in situ* or *operando* studies can be performed, involving (photo)(electro-)catalysis, batteries, photovoltaic materials, etc. A multi-technique approach is possible at Tarumã by combining the available techniques/detectors around the sample. Collecting simultaneously structural, electronic, and morphological pieces of information using these techniques (e.g. XAS, XRD, XRF) can pave the way for future contributions to electro-catalysis development.

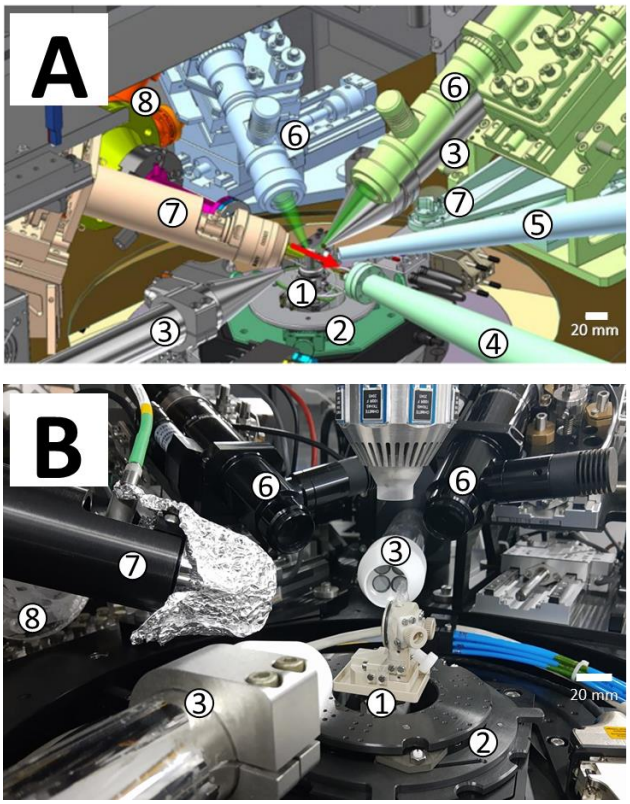

Figure 1. Engineering drawing (a) and picture (b) of the Tarumã experimental workstation, highlighting: the sample holder (1); the interface plate (2); the fluorescence detectors (3); the propagation cones for the PiMEGA (4) and MobiPix (5) X-rays area detectors; the optical microscopes (6); XEOL spectrometer (7); and the KB vacuum vessel (8). Adapted from the literature.[47]

XRF.

X-ray fluorescence is a non-destructive technique generally employed to determine the chemical composition of a sample. In XRF, the sample is illuminated by an X-ray source, causing them

to emit characteristic secondary X-rays.[51] Widely applied in synchrotron beamlines due to the tunability of the source and easy elemental distribution characterization, 2D maps (with nanometric resolution limited by the beam size) can be obtained by scanning the sample.[52] Besides the composition, the maps can be used for guiding the users, serving as a way to find a region of interest to be analyzed by other types of mapping analysis (like in XAS mapping, to get oxidation state maps as we will see in the following sections).

XAS and STXM.

X-ray Absorption Spectroscopy has been widely used for decades in the field of electrocatalysis.[53,54] XAS refers to the measurement of the absorption coefficient, which is directly related to the density and elemental composition of the sample. Therefore, it is an effective tool for identifying the sample's elements. As a spectroscopic tool, the fine control of the incident beam energy makes it possible to study the fine structure of the absorption coefficient as a function of the energy, which in turn makes it possible to identify selectively the element's chemical speciation[55,56] and the local structure composed by the nearest neighbors.[57,58] For the case of a focused beam, the spatial resolution can be exploited for mapping the transmitted beam, in what is known as Scanning Transmission X-ray Microscopy (STXM).[59–61] This image is a projection and therefore can be used to compose a tomographic acquisition allowing a three-dimensional mapping of the absorption spectrum.

PTYCHOGRAPHY and BCDI

Coherent diffraction imaging refers to a set of X-ray microscopy techniques that do not use lenses, but rather analyze the light coherently scattered by the sample to an area detector and use reconstruction algorithms to retrieve the phase of the scattered waves.[62] These techniques rely heavily on a coherent photon flux. The Carnaúba beam can approach a ratio of 100% coherent photons.

Ptychography is one of the most advanced X-ray microscopy techniques for high-resolution imaging, because it uses a focused beam in conjunction with its scanning over the sample making it suitable for large samples (with sizes ranging from some micrometers to millimeters) and it is compatible with other scanning microscopy and electrochemical systems.[63–65] This technique stands out not only for achieving a spatial resolution beyond the size of the focused beam.

Like ptychography, BCDI is an advanced imaging technique that can achieve a spatial resolution higher than the size of the focused beam. It analyzes the intensity modulation around a given Bragg peak making it suitable for (nano)crystalline samples, including (electro-)catalytic materials.[66] For BCDI, the sample must be smaller than the beam. The amplitude component refers to the electronic density projected in the direction of the Bragg peak and the phase to the stress field in the crystal lattice.[62]

(PHOTO)SPECTROELECTROCHEMICAL CELLS TO BE USED AT THE CARNAUBA BEAMLINE.

Coupling multiple techniques into electrochemical systems requires a cell that enables performing all available methods at the beamline and the electrochemical experiment. We have designed three different (photo)spectroelectrochemical cells for that purpose. We have included the term "photo" because most of the photoelectrochemical experiments are like the electrochemical ones, with the difference that a light source (solar simulators, LEDs, etc.) is placed in front of the working electrode while the electrochemical experiment is running. Hereafter, we shall refer to these cells as spectroelectrochemical cells (SECs) for brevity, although they can be utilized in photoelectrochemistry too. The purpose-built cells designed especially for the nanoprobe beamline were based on previous models (one used for several *in situ* techniques in our group,[67] and a microfluidic model designed for the Carnaúba beamline[68] after some improvements).

Apart from the electrochemical requirements of the cell (electrical contact, presence of an adequate electrolyte, etc.), it is worth noting that to take full advantage of the nanofocus, the beamline requires cells that meet its strict and challenging stability requirements associated with the focusing process.

X-RAY CELL

The cell in figure 2 works just like a typical electrochemical cell, but in a miniaturized form to fit the experimental hutch sample holder at the Carnaúba beamline. The cell is around 2 cm in size and weighs 50 g. It operates in reflection mode mounted on piezoelectric stages. Its cable routing was carefully planned not to disturb the experiment's mechanical stability. Despite the restrictions imposed by the stability requirements of the beamline, the cell design is still highly versatile. The working electrode (WE) consists of a rod of any solid (*e.g.*, Pt, Au, C) embedded in a polyether ether ketone (PEEK) such that only its tip comes into contact with the solution.[67] The counter electrode (CE) is a disk, which can also be made of any desired solid material and is easily removed from the cell body for cleaning. The reference electrode (RE) can also be made of various materials, as long as it fits the cell size requirements. In this case, we used a custom-made Ag/AgCl leak-free electrode with 1 mm diameter.

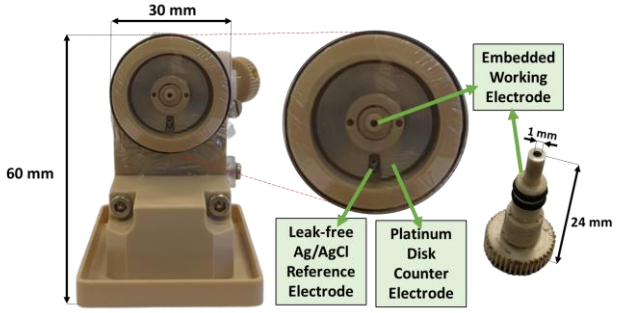

Figure 2. X-ray cell. It is designed to fit the beamline size and stability requirements. The body and connectors of the cell are made of PEEK. The electrolyte chamber is sealed by a thin mylar film held by an O-ring. The contact cables are carefully anchored to minimize vibrations. The figure also shows an enlarged image of the electrolyte compartment. The image permits observing the Pt WE and the RE tips and the Pt CE disk in more detail.

For *in situ* experiments, it is imperative to guarantee proper electrochemical behavior of the cell. Thus, our device was tested by using cyclic voltammetry (CV). We also performed the same experiment using the SEC WE in a conventional glass three-electrode electrochemical cell for comparison. We chose Pt as the electrode material for the characterization process because its electrochemical response is well-known, and it is the most used chemical element in (electro-)catalysis. We obtained the

electrode voltammetric profile in an H_2SO_4 solution (figure S1.A) and also performed some classical characterization experiments such as Cu underpotential deposition[69] (figure S1.B). The profiles not only show that the SEC response closely reproduces that of the glass cell, which is the goal of the SECs, but they are also in agreement with results from the literature.[70,71] This ensures the electrode's proper functioning and cleaning, since the voltammetric profile serves as a fingerprint of the electrochemical system. At this point, it is important to emphasize that we chose these reactions, instead of other more popular reactions like the ferricyanide-ferrocyanide couple, as these are much more sensitive to the cleaning quality of the system because the interaction between the reactant/products and the surface is much stronger in our choice.[72]

It is worth noting that for x-ray measurements we usually need to operate in thin layer mode, where the electrode is pressed against an X-ray transparent film to reduce the electrolyte layer thickness between the electrode and the polymer, minimizing the absorption of radiation by the electrolyte and thus decreasing the attenuation of the overall signal. However, this configuration likely increases the resistance of the electrolyte solution considerably (due to diffusion/migration restrictions), distorting the voltammetry profile (figure 3.A), as we thoroughly discussed elsewhere.[67] Fortunately, most modern potentiostats/galvanostats permit us to easily measure the uncompensated resistance (iR) and correct the potential applied online or after performing the experiment. Figure 3.B shows the impact of the iR correction in the CV response of the Pt electrode in a thin layer configuration. After correcting the applied potential, the results obtained with and without diffusion restrictions look much more similar. Overall, these measurements show that experiments performed in the conventional SEC are equivalent to those performed in a conventional three-electrode cell, making the comparison between experiments obtained in the laboratory and in the beamline reliable. Besides, we showed that, depending on the experiment, iR correction of the applied (or measured) electrochemical potential might be necessary.

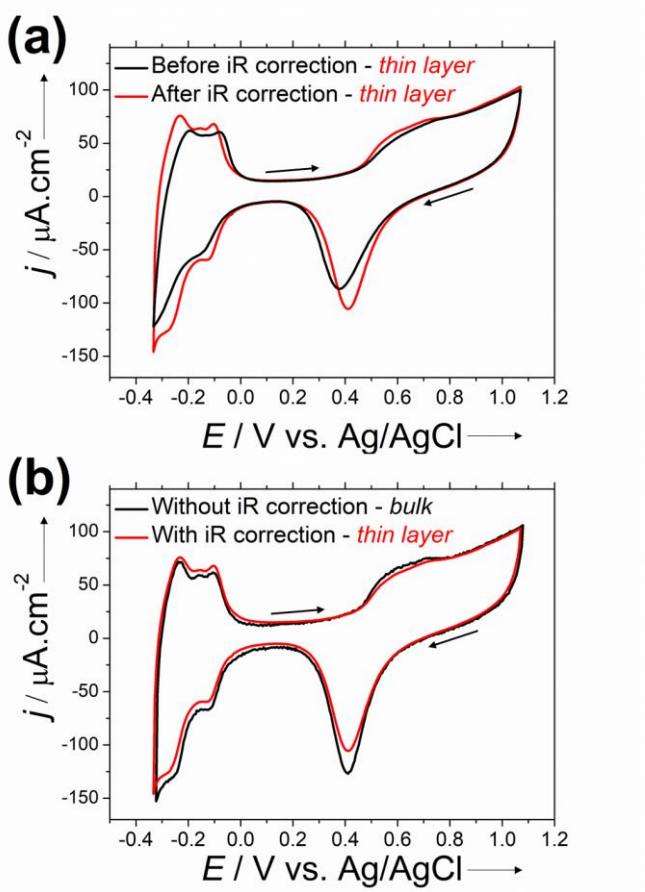

Figure 3. Electrochemical characterization experiments using the conventional SEC. All the experiments were performed using a Pt disk embedded in PEEK as WE, and in H_2SO_4 0.5 mol/L with a scan rate of 50 mV/s. (A) Blank profile obtained in thin layer mode both, before (black) and after (red) iR correction. It is clear that the profile gets significantly tilted if not corrected due to the high solution resistance caused by the thin layer of electrolyte. (B) Blank profile both in bulk (black) and in thin layer mode after iR correction (red). After iR correction, the profile is not distorted anymore, and the bulk profile is accurately recovered. The arrows indicate the sweep direction.

VIBRATIONAL SPECTROSCOPY CELL

To analyze the same electrode/material of interest using techniques other than X-rays, we developed a spectroelectrochemical cell for vibrational spectroscopy (figure 4.A) inspired by a previous development for *in situ* Fourier Transform Infrared (FTIR) spectroscopy, Raman, XAS, etc.[67] Even though we proved that our previous cell works well for several techniques, it was not able to fit exactly the same electrode used in the Carnaúba beamline, which is critical if the researchers aim for a direct comparison and/or spatial correlation between the results obtained with different techniques. Figure 4 shows two of the SECs we developed and highlights the working electrode that can be used on both of them. The vibrational spectroscopy cell is also made of PEEK, has a diameter of 4 cm, is 2.5 cm high, and also presents a three-electrode configuration. As we showed for the X-ray cell, this one uses the same working electrode, thus it also presents an electrochemical behavior similar to that of a glass electrochemical cell shown in Figure S1. Depending on the technique (Raman/FTIR), a quartz or CaF_2 window can be used to seal it.

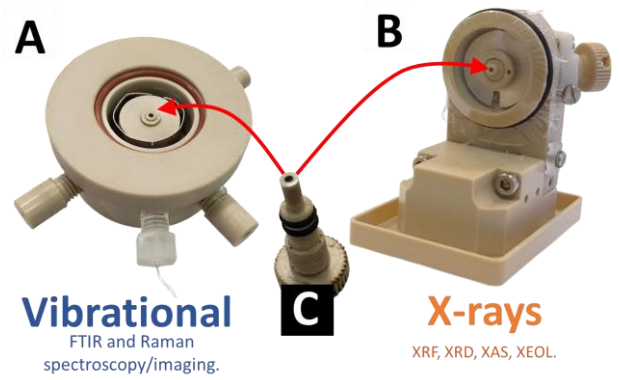

Figure 4. SECs developed for a multi-technique analysis of electrochemical systems. (A) Vibrational spectroscopy cell. (B) X-ray cell. (C) Working electrode used for both cells.

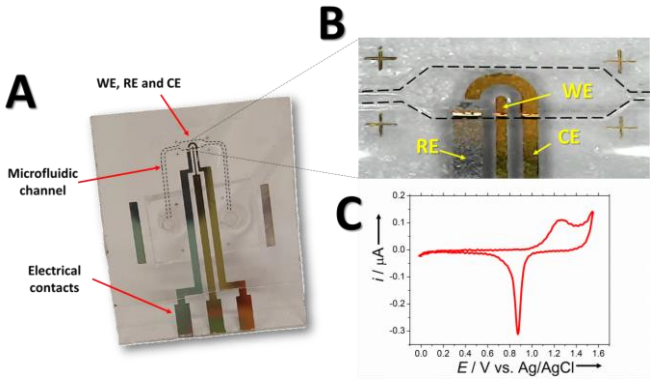

Figure 5. Microfluidic spectroelectrochemical cell. (A) 3D model showing the microfluidic cell components. (B) Photograph using a commercial bench microscope showing the zoomed-in microfluidic channel. Here, each electrode can be better visualized, and the channel borders are outlined for clarity. The WE/CE are gold electrodes, and the RE is a silver electrode where we deposit an Ag/AgCl layer. (C) Blank voltammogram of Au WE in $HClO_4$ 0.5 mol/L.

MICROFLUIDIC CELL

Having versatile devices which enable performing experiments in as many as possible sub-fields of electrochemistry is of paramount importance, as it expands the number of possible experiments which can exploit the nanoprobe beamline. Microfluidic cells have attracted the interest of the synchrotron community due to their reduced size, weight, high throughput, and compatibility with both *in situ* and *in vivo* experiments.[73–76] For this reason, we also developed a microfluidic SEC for X-ray analysis at SIRIUS, whose fabrication procedure was described in detail elsewhere.[68]

Briefly, the device consists of microchannels, and electrodes patterned by photolithography, sealed with a 12 μm thick layer of polyester film, which is highly transparent to X-rays above 7 keV (figure 5.A). This remarkably simple setup allows experiments using *in situ* X-ray diffraction (reflection mode) and absorption experiments, exploiting the fluorescence contrast.[77] The initial version consisted of three gold electrodes, which introduced some limitations, namely: i) the cell lacked a reliable reference electrode, which is mandatory for electrochemistry research[72] and ii) the similar size of the WE and CE could directly influence the current-potential response of the WE due to current limitations on the CE, which is a severe problem since most of the times the focus is on the WE, while the CE must simply act as an infinite source or sink of electrons.[78] To solve these issues, in this work we present a new model where we changed the electrode design and swapped one of the gold electrodes with a silver one. The new design (figure 5.B) solves the proportionality problem by using a CE bigger than the WE and provides a better electric field distribution around it by using a semicircle shape. Other modifications included changing the thickness of the electrodes (from 100 nm to around 1 μm) and the supporting material used to improve the adherence of the gold on the glass from Cr to Ti. We made these changes because it was observed that due to the presence of micrometric holes in the gold electrodes, formed during the lithography process and/or the potential cycling during the cleaning process, the electrolyte enters in contact with the Cr, dissolving it and causing the loss of electrical contact with the Au. In addition, one of the gold electrodes was made of silver to easily convert it into a pseudo-Ag/AgCl RE by chemically depositing an AgCl thin layer by immersing the electrode on a bleach solution, as described in the literature.[79] Only with a proper RE, the system is stable enough to get a voltammetric profile similar to that obtained in a regular glass cell.[80]

Cleaning the cell is necessary to remove the leftover contaminating species from the lithography fabrication process. In fundamental electrochemical studies using noble metal electrodes, the cleaning is straightforwardly performed by the traditional *flame annealing* process.[81] However, due to the sealing, this is not possible in this case, as a flame would destroy the polymers that make the device. Thus, the process was done by applying an extensive flow of ultrapure water followed by electrochemical cleaning of the electrode. The electrochemical cleaning consisted of cycling the cell rapidly in acidic media between the potentials where oxygen and hydrogen evolution currents can be observed in the voltammetry. Thus, by evolving gases on the electrodes in an aqueous electrolyte, the formation of adsorbed O and H removes the contaminations, which are then carried by the electrolyte flow. Lastly, it was characterized electrochemically using its blank voltammetric profile to check if the cell is working properly. After the cleaning process, the obtained profile is similar to that of polycrystalline gold electrodes in the same electrolyte[82] (figure 5.C) obtained in conventional glass cells.

EXPERIMENTAL RESULTS AT THE CARNAÚBA BEAMLINE.

XRF of Platinum structures deposited on glassy carbon

Nanoprobe beamlines were built to study a selected region of a given material (*i.e.*, a region containing a group of particles or, even a single NP) instead of measuring the average properties of the entire catalyst. One of the ways to correlate the composition, electronic properties, and electrochemical activity in a specific region of an electrode is first to perform an XRF map. The chemical composition map can be used to track features of the sample, such as its shape, which can be used to locate a target region.

XRF maps can be used to study increasingly smaller regions. For example, spherical platinum NPs (~5 nm in diameter) deposited on glassy carbon can be analyzed by XRF using different resolutions (figure 6.A-C), from covering a 250x250 μm^2 region, going down to a 5x5 μm^2 region with a total resolution (pixel size) of around 60 nm, making it possible to raster-scan the sample and localize the desired region with nanometer resolution. Moreover, XRF maps can also be used to examine the sample morphology,

instead of being used as a probe to locate specific features. For instance, figures 6.D and 6.E show images of Pt sputtered on a glassy carbon electrode with specific geometric shapes by using Focused Ion Beam (FIB). This surface was mapped by XRF (figure 6.D) and compared to a Scanning Electron Microscopy (SEM) image (figure 6.E) of the same region, showing an excellent correlation.

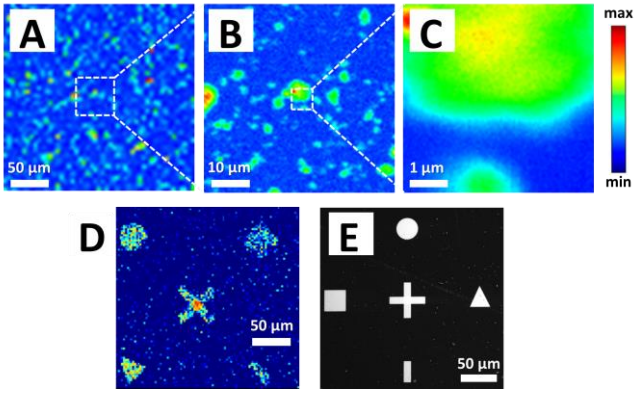

Figure 6. XRF maps for Pt L_3 edge. (A-C) Pt NPs deposit on a glassy carbon electrode with different resolutions, showing that depending on the sample, the beamline can adapt itself to the proper region of interest dimensions, all the way to a few micrometers regions and pixel size of around 60 nm. (D) FIB deposited Pt patterns. (E) SEM image of the Pt depositions shown in D for reference. The signal is more intense in regions where there is a higher concentration of Pt. Despite the pixel size, the technique resolution is still limited by the beam size. If the pixel is smaller than the beam, the sample will be measured more than once, not increasing the overall resolution, but improving the image contrast.

XRF mapping enables us to get spatially resolved images of the (electro-)catalyst with different magnifications, covering a wide size range, from micrometric to nanometric materials. More importantly, it can be performed *in situ,* allowing us to get images of the material morphology during (electro-)catalytic reactions with similar accuracy to SEM, as it can be seen by comparing figure 6D and 6E. Lastly, it permits the visualization of the chemical element distribution, which is extremely important in the (electro-)catalysis field, allowing us to understand changes in activity and stability of the analyzed surface.

XAS of Platinum NPs deposited on glassy carbon

X-ray absorption can also be performed at the Carnaúba beamline with nanoscale spatial resolution, yielding maps carrying information about the electronic structure or oxidation state. XAS experiments can be performed at both EXAFS (Extended X-ray Absorption Fine Structure) and XANES (X-ray Absorption Near Edge Structure) modes. In contrast to the usual XAS analysis, which is performed with beam sizes in the order of micrometers to millimeters,[83,84] and thus provides the average response from many NPs in the case of nanomaterials, by using a nanoprobe it is possible to analyze features from small clusters down to single NPs. This approach might show a different behavior than that observed with usual XAS, depending on which area of the sample is analyzed.

Even though the XAS analysis is performed with higher spatial resolution than in conventional measurements (irradiating smaller areas means that we irradiate less absorbers and then increase the technique sensitivity), thanks to the higher flux provided by a 4th generation synchrotron source, we are still capable of obtaining adequate signal-to-noise ratio (Figure 7.A). To define the desired region of interest and characterize the sample as shown in the previous section, the surface is first mapped by XRF, which allows the scientist to choose a region of interest to study. Then, using the beamline fine control of the beam position, the beam can be focused exactly on the desired position to collect the XAS data. It is important to note that the signal comes from only the region under the X-ray beam irradiation cross-section (figure 7.B). At Carnaúba, the beam size is currently around 150x450 nm^2, but future improvements should decrease its size at the Tarumã station to 150x150 nm^2. This opens up many experimental possibilities. One can, for example, get XAS spectra at different regions and then collect a map correlating any of the data extracted from it (*e.g.*, oxidation state) with the material morphology for a spatially resolved analysis, instead of just a single point average interpretation of the problem.

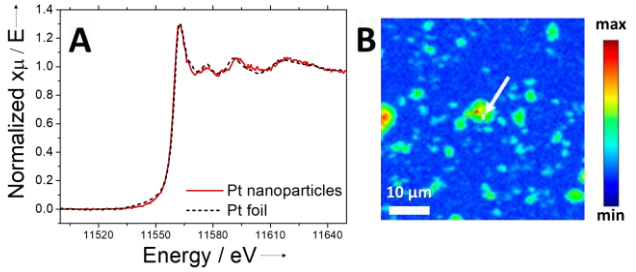

Figure 7. (A) XANES normalized spectrum for Pt L_3 edge for a reference Pt foil and Pt NPs deposited on GC substrate. (B) XRF map of the Pt NPs. The signal is collected only in the central region of the fluorescence map, as indicated by the white spot with the pointing arrow. The beam cross-section is not in scale.

BCDI of shape-controlled Platinum NPs

Measuring the morphological properties and/or activity of single NPs could pave the way for a deeper understanding of the correlation between the structure and activity of individual particles. For more details about the potential contributions of this technique to electrocatalysis, how to perform the measurements and the physics behind it, we refer the readers to a contribution of some of us.[66] Despite the experimental difficulties faced when combining electrochemistry and BCDI, Maillard et al. have recently published the first article in electrocatalysis.[85] This seminal article in the field of (electro-)catalysis brings new information but, more importantly, shows the countless possibilities this technique offers to the field, however, still with the limitations of studying relatively big nanoparticles (240×230×110 nm^3) and in a narrow potential window.

This kind of single NP experiments can enormously contribute to comprehending the correlation between particle structural features and the average response of NP electrocatalysts obtained by conventional electrochemical measurements. In this context, many techniques do well at sensing activity/selectivity of single NPs, among which there are many microscopy methods (Scanning Electrochemical Microscopy (SECM), Scanning Ion-conductance Microscopy (SICM), Dark-field Microscopy (DFM), Plasmonic-based Electrochemical Current Microscopy (P-ECM), etc.)[44,86,87] and nanoconfinement techniques (ultramicroelectrodes, nanoelectrodes, single NP collision, nanopores, nanochannels, etc.).[44,88,89] Besides the aforementioned techniques, an appealing technique for single NP analysis, especially for (electro-)catalysis is the Scanning Electrochemical Cell Microscopy (SECCM), which permits correlating structure/function in the nanoscale *in*

situ/operando.[90–92] At last, we can also mention Scanning Tunneling Microscopy (STM), Atomic Force Microscopy (AFM), and High-resolution Transmission Electron Microscopy (HR-TEM), which can also provide nanoscale, or even atomic, resolution. These last three are versatile tools that permit to observe materials at the nanoscale with higher detail, but, on the other hand they do not permit measuring electrochemical activity. Nanoconfinement experiments and SECCM allow measuring electrochemical activity, but they do not provide information about the structure of the particles. In this context, BCDI is a potentially powerful technique to explore electrocatalysts,[66] as it can be performed *in situ* with the right experimental setup, providing complementary information to the more well-developed techniques mentioned before.

At Carnaúba, using the cells we developed, it is already possible to reconstruct the tridimensional shape of a single nanocrystal of the electrocatalyst. For instance, in figure 8, we show the reconstruction for a Pt nanocrystal. Figures 8.A-1 and 8.A-2 show the nanofluorescence and nanodiffraction maps acquired simultaneously, which allows finding the region of interest for 3D imaging. The pixel size in the XRF corresponds to the integrated spectra over the Pt fluorescence (SSD detector), on the other hand, the XRD map is the integration of the area detector intensity at the Bragg peak (Pt 111). Figures 8.A-3 to 8.A-5 show three slices of the reciprocal space obtained during the rocking curve, *i.e.,* rotating the cell as shown in figure 8.B-1. In this measurement the reciprocal space was mapped in steps of 0.003° covering an angular range of ± 0.5° under 10^9 photons/sec. Figure 8.B-2 shows a simplified schematic of the reconstruction algorithm of phase retrieval. The 3D image shown was obtained using the pyNX code developed on the ESRF.[93] The Pt NPs were synthesized electrochemically[94] and exposed to a heat treatment (450°C for 15min) before the data collection to minimize defects associated with the electrochemical growth. The reconstructed particle closely resembles the particle shape after the heat treatment (figure S2), which noticeably affects the particle edges. The particle obtained is around 85 nm, which agrees with the average particle size measured using electron microscopy (figure S3). Finally, it is important to highlight that these proof-of-concept experiments show enormous advances. At least to our knowledge, we are extremely close to the current size limit for a tridimensional reconstruction. Including this work, there are other two reports with full tridimensional reconstructions using particles in the same size range (from 45 to 60 nm), a recent pre-print publication of Björling et al.[95] and another previous work from the same author,[96] showing the smallest particles imaged with the technique so far. This demonstrates that we can get images *in situ* of particles with sizes well below 100 nm, which has been one of the main drawbacks of the technique for its application in the field of (electro-)catalysis. It is worth mentioning that Richard et al. have been able to image 20 nm Pt NPs using the recently upgraded extremely brilliant source (EBS),[97] but they didn't publish a complete 3D reconstruction, although they were able to image the same particle from different angles.

To end this section, we would like to highlight the work of Björling et al.,[95] describing in detail some problems that might be generated by the x-ray beam. As in our previous publication,[66] we would like to emphasize the importance of control experiments again. Besides, microfluidic cells such as the one we showed here could contribute to mitigate these problems by adjusting the flux and temperature of the electrolyte.

SPECTROSCOPIC APPROACH.

To contribute to the development of the field of (electro-)catalysts, it is important to correlate structural/compositional information with activity, selectivity and stability, as each of these properties is intricately connected.[98] Therefore, if one uses a characterization technique that provides information about only one of these aspects, the results must be supplemented to get a complete view of the catalyst performance. The usage of x-rays may excel at structure and stability analysis (by tracking the material morphology and structure over time), but it lacks the ability to evaluate activity and selectivity. On the other hand, spectroscopic techniques such as *in situ* FTIR and Raman are compelling at probing selectivity/activity.[99–101] Vibrational spectroscopy can be used to analyze key species at the electrical double layer, including the electrocatalytic material,[102] adsorbate-electrode intermediate species,[103] and also reaction products.[104] In addition, this information can be used in time-dependent studies to infer the (electro-)catalyst stability.[105]

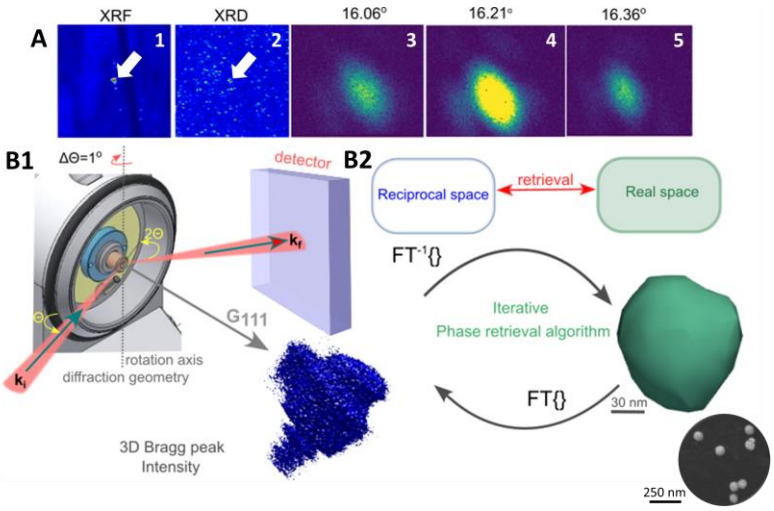

Figure 8. (A.1) Bidimensional XRF and (A.2) XRD maps around the analyzed sample (shown by a white arrow). (A.3-5) Diffraction patterns at Pt 111 Bragg peak (16.21°), and ± 0.15° around it, in the reciprocal space. (B1) The figure shows how the reconstruction can be obtained: the sample is rotated about 1° around an

axis in the plane of the crystallographic plane to be analyzed. The scattering vector (G_{111}) is perpendicular to the crystallographic plane of interest. The incident wave (k_i) hits the sample, and the diffracted wave (k_f) goes to the detector. Then, the diffraction patterns at different angles (as the ones shown in A) are combined to get a tridimensional Bragg peak diffraction intensity (in blue). (B.2) To get the reconstructed shape (in green), the reciprocal space data goes through a phase retrieval process to recover the real space information. An iterative phase retrieval algorithm converts the real and reciprocal space data by consecutive Fourier transforms. The SEM image of the analyzed crystals is shown in the inset.

If we correlate spatially resolved data coming from X-ray-based techniques with a spectroscopy analysis which is not also spatially resolved, it would be difficult to do any correlation between the spectroscopic results and the X-ray-based characterization. In this case, a spatially resolved spectroscopic analysis would permit to take full advantage of the also spatially resolved X-ray experiment. By analyzing a heterogeneous structure using spatially resolved vibrational spectroscopy, the questions that we might want to answer would be: Is the activity homogeneous in the whole structure? What are the main products of the reaction? Is the selectivity homogeneous, i.e., are the same products formed in the different “points” in a given analyzed region?

FTIR imaging can be used to track both activity and selectivity. For example, in the case of glycerol electro-oxidation, the stretching bands due to the oxidation products (like carbonyl containing groups, or even carbon monoxide/dioxide) allow the observation of where the reaction takes place (figure 9) and how intense is the reaction at different regions. The selectivity can be inferred by comparing the intensity from different bands, which might be different depending on the mechanism taking place at each region of the catalyst. Raman microscopy, on the other hand, can be used to probe either the catalyst or surface-adsorbed molecules through the observation of characteristic bond vibrations.[106] In cases where the substrate contains Raman active bands (such as the carbon, in our case), and the catalyst itself does not, it can be used to track the catalyst distribution (figure 9).

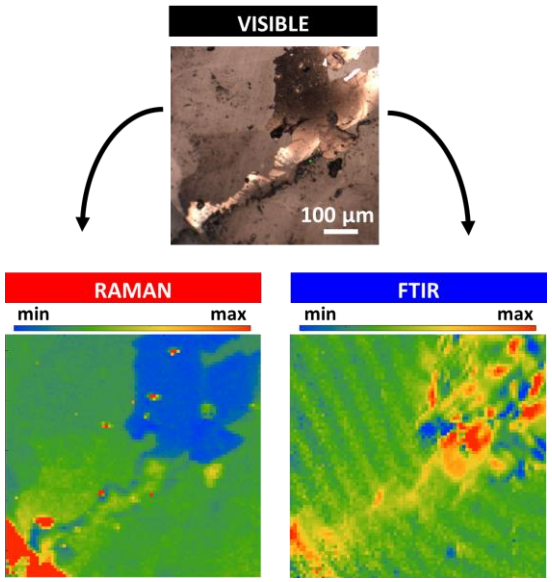

Figure 9. Visible image and spatially resolved vibrational spectroscopy images for a patterned Pt deposition over a GC substrate. The visible image (top) shows a shining Pt deposit on an opaque background. The Raman map is shown in the bottom left. The map was obtained using the G band of C at 1600 cm^{-1} Raman shift. The Pt Raman signal is very low, thus the regions where there is Pt over the C attenuate the signal, providing the contrast to map the morphology of the catalyst. The same catalyst was then used for glycerol oxidation in acidic media. During the oxidation, FTIR images were collected at different applied potentials in a 0.1 mol/L perchloric acid solution. The result at 1 V vs. RHE is shown in the bottom right using the carbonyl band at 1740 cm^{-1}. Many oxidation products contain carbonyl groups, thus using this band enables following the activity at different regions of the catalyst. The average FTIR and Raman spectrum and some point spectra for different regions of the sample are shown in Figure S4 and S5, respectively.

The FTIR/Raman maps can then be correlated with the ones obtained using X-rays, such as XRF, providing insights into the structure-activity correlation by connecting the information about activity/selectivity with the morphological/structural data. Of course, this is true provided that we can use different techniques at the same region of interest, which shows why the development of an experimental setup for this is relevant. Moreover, it is important to note that spatially resolved FTIR/Raman allows getting the information carried by conventional spectroscopic analysis (the signal in this case is the average from all pixels collected by the infrared beam), besides the spatially resolved data itself. This is relevant for heterogeneous micro or nanoscale (electro-)catalyst structures, because when the signal coming from all pixels is averaged, important details might be lost in the process (when a low signal response gets even lower when averaged). This can be noticed in the FTIR imaging of Pt catalysts, where the CO band is not visible in the average spectrum, but it is noticeable in a pixel spectrum (figure S6).

Unfortunately, FTIR and Raman have resolutions around hundreds or thousands of nanometers, which is not suitable for many systems. For instance, if we have particles of around 10 nm, with average distances of 100 nm we will not be able to differentiate signals coming from individual NPs with these two spectroscopies. Thus, we believe that Scanning Electrochemical Microscopy (SECM),[35,107–109] and its analogs, which can reach nanoscale resolution, could be excellent techniques to be coupled with some of Carnauba´s characterization tools discussed here. Using this method, the activity can also be probed *in situ* by measuring the electro-oxidation current directly or indirectly by performing a selective electro-oxidation reaction of a product, instead of spectroscopically monitoring the reaction products. However, vibrational spectroscopy is easier to perform, and even though the resolution is lower, these techniques are useful for many systems which do not require nanometric resolution. Besides, spectroscopic approaches are better than SECM-related techniques to simultaneously identify different products. Finally, it is important to note that these developments can be used in new[110] and future technologies able to reach a higher spatial resolution. For instance, in Optical Photothermal IR (O-PTIR), by using a photothermal effect to detect the infrared absorption, it is possible to reach resolutions well below 1 µm depending on the laser used.[110]

Conclusion and Perspectives

In this work, we described several techniques that permit to characterize *(in situ* or *ex situ*) catalytic surfaces or measure their electrochemical activity with spatial resolution, which is essential for analyzing heterogeneous structures. Real (electro-)catalysts are composed of a range of particle/grain sizes, hence presenting some dispersion in their shape, composition, etc. Since the response of these materials is the product of a combination of

many interrelated intrinsic characteristics of the sample, it makes it difficult to separate the contribution of all these effects in different regions.[111] For example, in the electrochemistry field, it is not hard to find studies where the structure of a material is evaluated by high-resolution techniques (such as TEM), then the response of this specific analyzed region is directly assigned to the whole sample, which is not necessarily homogeneous. For this reason, it is extremely important to develop new techniques, or combination of them, which can enable the correlation of the structure of the catalyst with the activity/selectivity of the reactions using parameters that have been historically measured as average values (like the oxidation state of atoms, coordination number, structure around an atom, etc.). With the aid of 4th generation synchrotrons, now many of these parameters can be mapped with nanometric resolution.

This kind of combination have been limited to a few research groups due to the lack of instrumentation to combine different techniques which have a relatively high cost or require very specialized human resources to run them and/or to build the necessary facility. However, equipment such as FTIR and Raman microscopes are becoming more and more popular, to a point where nowadays there are several available commercial microscopes with different prices and performances, that allow getting results similar to those shown here. Besides, new technologies are emerging, improving both the sensitivity and resolution of these techniques.[110,112]

This fancy set of techniques allows obtaining unique results and it will certainly help push the border of knowledge in several fields of science and technology. Unfortunately, nanofocus beamlines are not as available as the other resources mentioned here, but the future is promising. The first 4th generation nanofocus beamline was set at MAX IV in 2016,[113] then, ESRF launched its beamline upgrade in 2018[114] and Sirius started commissioning its first in 2021[48] (many others are in the planning stage, new facilities like HEPS in China, or upgrades to existing ones such as APS-U in the USA, PETRA IV in Germany, ELETTRA 2.0 in Italy, to cite some[115]). Thus, the development of tools and training of human resources to take advantage of these facilities is extremely important not only for the beamlines we have today, but also for the many available soon.

We have developed some experimental setups and we showed here just a flavor of how several techniques can be combined. We hope that researchers all over the world take advantage of these tool to tackle relevant electrochemical problems. Even if we have focused mainly on one-element NPs or heterogeneous structures (nano or micro), some of the techniques and tools presented here can be useful to study for instance multicomponent catalysts,[116–120] from multimetallic particles to high entropy alloys (HEAs). In these cases, getting to know how the activity/selectivity is connected to the structure/element distribution is especially important, since this is key to understand how each component determines the overall electrocatalytic activity.[107]

The biggest limitation of using the proposed combination of techniques is the resolution difference between them. While X-ray techniques available at the Carnaúba beamline can reach a nanoscale resolution, for most FTIR imaging and Raman microscopy equipment, the resolution is limited to the micrometer scale. However, our aim here was to show the instrumentation we developed and its functioning through some proof-of-concept experiments. Besides, we highlighted the value of combining different techniques, which is not restricted to the combinations done here. For instance, a group with expertise in SECM can use a nanoprobe beamline to characterize a surface and the SECM to correlate the outputs of the characterization with the activity. Therefore, by showing these examples and the facilities available at the Carnauba beamline, we hope to have encouraged researchers to plan ambitious experiments in their fields, able to obtain new and relevant information through a multi-technique approach.

Experimental Section

Electrochemical experiments. The electrochemical experiments (such as the electro-oxidation of glycerol) were performed by using cyclic voltammetry (CV), and chronoamperometry. We used a Metrohm potentiostat (Autolab PGSTAT302N). When at the Carnaúba beamline, the potentiostat used was a device built/programmed by the beamline staff. The CV experiments were performed in the three-electrode spectroelectrochemical cells. The voltammogram profiles were performed at current sweep a rate of 50 mV/s in the potential range from 0.05V to 1.45V vs. the reversible hydrogen electrode (RHE). The solutions were prepared using the following chemicals: sodium hydroxide (Sigma-Aldrich®, 99.99%) and perchloric acid (Sigma-Aldrich®, 70-72%, EMSURE®). Solutions were prepared using ultrapure water (Milli-Q, 18.2 MΩ). Prior to the experiments the glassy carbon substrates were polished using increasingly finer sandpaper (p2500 to p4000) and then alumina powder (0.3 μm) over a wet polishing cloth. The Pt electrodes were cleaned using flame annealing. The oxygen was removed from the solutions by nitrogen purging before the experiments.

X-ray experiments at Carnaúba. The 2D XRF maps were obtained using a 12 keV energy. The XANES analysis used an energy range from 11 keV to 11.65 keV, with steps of 0.5 eV. The diffraction patterns were collected at 9.725 keV (λ=1.27 nm), these patterns are the input used for the BCDI reconstruction to map the 3D Bragg peak intensity,

Spatially resolved FTIR and Raman. The FTIR spectra were collected using a Cary 670 (Agilent) spectrometer. The maps were collected using a spectral resolution of 8 cm^{-1} and spatial resolution of around 3 μm, collecting a total of 512 interferograms. The Raman spectra were collected using a XploRA ONE (Horiba) confocal microscope. Each map was performed using 2s acquisition time and 2 spectra accumulation. We used a 785 nm laser. The image was collected by scanning the sample in point-by-point mode, with each point of the map being spaced from each other (vertically and horizontally) by 5 μm.

Acknowledgments

This research was funded by Fundação de Amparo à Pesquisa do Estado de São Paulo (FAPESP) (grants: 2017/11986-5, 2020/04431-0, 2020/07955-0, and 2021/02678-0), and by the Coordenação de Aperfeiçoamento de Pessoal de Nível Superior (CAPES) (grant: 653684/2021-00). The authors thank the support from Shell and the strategic importance of the support given by ANP (Brazil's National Oil, Natural Gas and Biofuels Agency) through the R&D levy regulation. This research used resources of the Brazilian Synchrotron Light Laboratory (LNLS), part of the Brazilian Center for Research in Energy and Materials (CNPEM), a private non-profit organization under the supervision of the Brazilian Ministry for Science, Technology, and Innovations (MCTI). The Carnaúba beamline staff is

acknowledged for the assistance during the experiments (20210015).

Keywords: electrochemistry • spectro-electrochemistry • imaging • multi-technique • nanoprobe beamline

References

[1] Z. J. Xu, X. Wang, *Chem. - A Eur. J.* **2020**, 100084.

[2] O. A. Ibrahim, M. Navarro-Segarra, P. Sadeghi, N. Sabaté, J. P. Esquivel, E. Kjeang, *Chem. Rev.* **2022**, *122*, 7236–7266.

[3] Ermete Antolini, *Catalysts* **2019**, 980.

[4] C. Coutanceau, S. Baranton, *Wiley Interdiscip. Rev. Energy Environ.* **2016**, *5*, 388–400.

[5] N. P. Martínez, M. Isaacs, K. K. Nanda, *New J. Chem.* **2020**, *44*, 5617–5637.

[6] M. Younas, S. Shafique, A. Hafeez, F. Javed, F. Rehman, *Fuel* **2022**, *316*, 123317.

[7] R. L. Borup, A. Kusoglu, K. C. Neyerlin, R. Mukundan, R. K. Ahluwalia, D. A. Cullen, K. L. More, A. Z. Weber, D. J. Myers, *Curr. Opin. Electrochem.* **2020**, *21*, 192–200.

[8] R. Abbasi, B. P. Setzler, S. Lin, J. Wang, Y. Zhao, H. Xu, B. Pivovar, B. Tian, X. Chen, G. Wu, Y. Yan, *Adv. Mater.* **2019**, *31*, 1–14.

[9] D. A. Cullen, K. C. Neyerlin, R. K. Ahluwalia, R. Mukundan, K. L. More, R. L. Borup, A. Z. Weber, D. J. Myers, A. Kusoglu, *Nat. Energy* **2021**, *6*, 462–474.

[10] C. L. Bentley, M. Kang, P. R. Unwin, *J. Am. Chem. Soc.* **2019**, *141*, 2179–2193.

[11] C. H. Ryu, H. Lee, H. Lee, H. Ren, *J. Phys. Chem. Lett.* **2022**, *13*, 7838–7846.

[12] F. Calle-Vallejo, M. D. Pohl, D. Reinisch, D. Loffreda, P. Sautet, A. S. Bandarenka, *Chem. Sci.* **2017**, *8*, 2283–2289.

[13] F. Calle-Vallejo, J. Tymoczko, V. Colic, Q. H. Vu, M. D. Pohl, K. Morgenstern, D. Loffreda, P. Sautet, W. Schuhmann, A. S. Bandarenka, *Science (80-.).* **2015**, *350*, 185–189.

[14] L. Godeffroy, J. F. Lemineur, V. Shkirskiy, M. Miranda Vieira, J. M. Noël, F. Kanoufi, *Small Methods* **2022**, *6*, 1–12.

[15] R. Narayanan, M. A. El-Sayed, *Nano Lett.* **2004**, *4*, 1343–1348.

[16] N. S. Porter, H. Wu, Z. Quan, J. Fang, *Acc. Chem. Res.* **2013**, *46*, 1867–1877.

[17] H. Zhang, M. Jin, Y. Xiong, B. Lim, Y. Xia, *Acc. Chem. Res.* **2013**, *46*, 1783–1794.

[18] J. Solla-Gullón, F. J. Vidal-Iglesias, A. López-Cudero, E. Garnier, J. M. Feliu, A. Aldaz, *Phys. Chem. Chem. Phys.* **2008**, *10*, 3689.

[19] K. M. Bratlie, H. Lee, K. Komvopoulos, P. Yang, G. A. Somorjai, *Nano Lett.* **2007**, *7*, 3097–3101.

[20] B. Wu, N. Zheng, *Nano Today* **2013**, *8*, 168–197.

[21] Z. Y. Zhou, N. Tian, J. T. Li, I. Broadwell, S. G. Sun, *Chem. Soc. Rev.* **2011**, *40*, 4167–4185.

[22] T. Sheng, Y. F. Xu, Y. X. Jiang, L. Huang, N. Tian, Z. Y. Zhou, I. Broadwell, S. G. Sun, *Acc. Chem. Res.* **2016**, *49*, 2569–2577.

[23] B. E. Hayden, *Acc. Chem. Res.* **2013**, *46*, 1858–1866.

[24] A. A. Vertegel, R. W. Siegel, J. S. Dordick, *Langmuir* **2004**, *20*, 6800–6807.

[25] J. Jiang, G. Oberdörster, A. Elder, R. Gelein, P. Mercer, P. Biswas, *Nanotoxicology* **2008**, *2*, 33–42.

[26] W. Tang, H. Lin, A. Kleiman-Shwarsctein, G. D. Stucky, E. W. McFarland, *J. Phys. Chem. C* **2008**, *112*, 10515–10519.

[27] V. Climent, J. M. Feliu, *J. Solid State Electrochem.* **2011**, *15*, 1297–1315.

[28] G. Soffiati, J. L. Bott-Neto, V. Y. Yukuhiro, C. T. G. V. M. T. Pires, C. C. Lima, C. R. Zanata, Y. Y. Birdja, M. T. M. Koper, M. A. San-Miguel, P. S. Fernández, *J. Phys. Chem. C* **2020**, acs.jpcc.0c05017.

[29] B. D. B. Aaronson, C. H. Chen, H. Li, M. T. M. Koper, S. C. S. Lai, P. R. Unwin, *J. Am. Chem. Soc.* **2013**, *135*, 3873–3880.

[30] M. R. S. Soares, C. A. R. Costa, E. M. Lanzoni, J. Bettini, C. A. O. Ramirez, F. L. Souza, E. Longo, E. R. Leite, *Adv. Electron. Mater.* **2019**, *5*, 1–8.

[31] S. C. Paul, S. C. Dey, M. A. I. Molla, M. S. Islam, S. Debnath, M. Y. Miah, M. Ashaduzzaman, M. Sarker, *Polyhedron* **2021**, *193*, 114871.

[32] X. Chen, C. Li, M. Grätzel, R. Kostecki, S. S. Mao, *Chem. Soc. Rev.* **2012**, *41*, 7909–7937.

[33] N. Sharma, H. Ojha, A. Bharadwaj, D. P. Pathak, R. K. Sharma, *RSC Adv.* **2015**, *5*, 53381–53403.

[34] F. Zaera, *Chem. Soc. Rev.* **2013**, *42*, 2746–2762.

[35] D. Martín-Yerga, M. Kang, P. R. Unwin, *ChemElectroChem* **2021**, *8*, 4240–4251.

[36] M. T. M. Koper, J. J. Lukkien, N. P. Lebedeva, J. M. Feliu, R. A. Van Santen, *Surf. Sci.* **2001**, *478*, DOI 10.1016/S0039-6028(01)00957-8.

[37] R. M. Arán-Ais, F. J. Vidal-Iglesias, M. J. S. Farias, J. Solla-Gullón, V. Montiel, E. Herrero, J. M. Feliu, *J. Electroanal. Chem.* **2017**, *793*, 126–136.

[38] F. Maillard, S. Schreier, M. Hanzlik, E. R. Savinova, S. Weinkauf, U. Stimming, *Phys. Chem. Chem. Phys.* **2005**, 375–383.

[39] A. López-Cudero, J. Solla-Gullón, E. Herrero, A. Aldaz, J. M. Feliu, *J. Electroanal. Chem.* **2010**, *644*, 117–126.

[40] R. De Marco, J. P. Veder, *TrAC - Trends Anal. Chem.* **2010**, *29*, 528–537.

[41] T. Iwasita, F. . Nart, *Prog. Surf. Sci.* **1997**, *55*, 271–340.

[42] Z. Q. Tian, B. Ren, *Annu. Rev. Phys. Chem.* **2004**, *55*, 197–229.

[43] X. Li, H.-Y. Wang, H. Yang, W. Cai, S. Liu, B. Liu, *Small Methods* **2018**, *2*, 1700395.

[44] Y. Wang, X. Shan, N. Tao, *Faraday Discuss.* **2016**, *193*, 9–39.

[45] S. E. F. Kleijn, S. C. S. Lai, M. T. M. Koper, P. R. Unwin, *Angew. Chemie - Int. Ed.* **2014**, *53*, 3558–3586.

[46] Y. Zhu, J. Wang, H. Chu, Y. C. Chu, H. M. Chen, *ACS Energy Lett.* **2020**, *5*, 1281–1291.

[47] H. C. N. Tolentino, R. R. Geraldes, G. B. Z. L. Moreno, A. C. Pinto, C. S. N. C. Bueno, L. M. Kofukuda, A. P. S. Sotero, A. C. P. Neto, F. R. Lena, W. H. Wilendorf, in *X-Ray Nanoimaging Instruments Methods V*, International Society For Optics And Photonics, **2021**, p. 1183904.

[48] H. C. N. Tolentino, M. M. Soares, C. A. Perez, F. C. Vicentin, D. B. Abdala, D. Galante, V. D. C. Teixeira, D. H. C. De Araujo, H. Westfahl, *J. Phys. Conf. Ser.* **2017**, *849*, DOI 10.1088/1742-6596/849/1/012057.

[49] L. Mino, E. Borfecchia, J. Segura-Ruiz, C. Giannini, G. Martinez-Criado, C. Lamberti, *Rev. Mod. Phys.* **2018**, *90*, 25007.

[50] C. A. Perez, H. C. N. Tolentino, M. M. Soares, C. S. B. Dias, D. Galante, V. de C. Teixeira, D. Abdala, H. Westfahl, *Microsc. Microanal.* **2018**, *24*, 330–331.

[51] K. W. Jones, B. M. Gordon, A. L. Hanson, W. M. Kwiatek, J. G. Pounds, *Ultramicroscopy* **1988**, *24*, 313–328.

[52] J. A. Barbosa, V. M. S. Freitas, L. H. B. Vidotto, G. R. Schleder, R.

A. G. De Oliveira, J. F. Da Rocha, L. T. Kubota, L. C. S. Vieira, H. C. N. Tolentino, I. T. Neckel, A. L. Gobbi, M. Santhiago, R. S. Lima, *ACS Appl. Mater. Interfaces* **2022**, DOI 10.1021/acsami.2c02943.

[53] J. Timoshenko, B. Roldan Cuenya, *Chem. Rev.* **2021**, *121*, 882–961.

[54] M. Wang, L. Árnadóttir, Z. J. Xu, Z. Feng, *Nano-Micro Lett.* **2019**, *11*, 1–18.

[55] F. Poineau, M. Fattahi, C. Den Auwer, C. Hennig, B. Grambow, *Radiochim. Acta* **2006**, *94*, 283–289.

[56] F. J. Zhao, K. L. Moore, E. Lombi, Y. G. Zhu, *Trends Plant Sci.* **2014**, *19*, 183–192.

[57] R. Dominko, I. Arčon, A. Kodre, D. Hanžel, M. Gaberšček, *J. Power Sources* **2009**, *189*, 51–58.

[58] S. Mukerjee, J. McBreen, *J. Electroanal. Chem.* **1998**, *448*, 163–171.

[59] D. Guay, J. Stewart-Ornstein, X. Zhang, A. P. Hitchcock, *Anal. Chem.* **2005**, *77*, 3479–3487.

[60] F. M. F. de Groot, E. de Smit, M. M. van Schooneveld, L. R. Aramburo, B. M. Weckhuysen, *ChemPhysChem* **2010**, *11*, 951–962.

[61] E. De Smit, I. Swart, J. F. Creemer, G. H. Hoveling, M. K. Gilles, T. Tyliszczak, P. J. Kooyman, H. W. Zandbergen, C. Morin, B. M. Weckhuysen, F. M. F. De Groot, *Nature* **2008**, *456*, 222–225.

[62] I. Robinson, R. Harder, *Nat. Mater.* **2009**, *8*, 291–298.

[63] B. Bozzini, G. Kourousias, A. Gianoncelli, M. W. M. Jones, G. Van Riessen, M. Kiskinova, *J. Electron Spectros. Relat. Phenomena* **2017**, *220*, 147–155.

[64] G. Kourousias, B. Bozzini, M. W. M. Jones, G. A. Van Riessen, S. Dal Zilio, F. Billè, M. Kiskinova, A. Gianoncelli, *Appl. Nanosci.* **2018**, *8*, 627–636.

[65] M. Abe, F. Kaneko, N. Ishiguro, T. Kubo, F. Chujo, Y. Tamenori, H. Kishimoto, Y. Takahashi, *J. Phys. Chem. C* **2022**, *126*, 14047–14057.

[66] R. A. Vicente, I. T. Neckel, S. K. R. S. Sankaranarayanan, J. Solla-Gullon, P. S. Fernández, *ACS Nano* **2021**, DOI 10.1021/acsnano.1c01080.

[67] J. L. Bott-Neto, M. V. F. Rodrigues, M. C. Silva, E. B. Carneiro-Neto, G. Wosiak, J. C. Mauricio, E. C. Pereira, S. J. A. Figueroa, P. S. Fernández, *ChemElectroChem* **2020**, *7*, 4306–4313.

[68] I. T. Neckel, L. F. de Castro, F. Callefo, V. C. Teixeira, A. L. Gobbi, M. H. Piazzetta, R. A. G. de Oliveira, R. S. Lima, R. A. Vicente, D. Galante, H. C. N. Tolentino, *Sci. Rep.* **2021**, *11*, 1–11.

[69] O. A. Oviedo, L. Reinaudi, S. Garcia, E. P. M. Leiva, *Underpotential Deposition*, **2016**.

[70] M. W. Breiter, *J. Electrochem. Soc.* **1967**, *114*, 1125.

[71] G. Jerkiewicz, G. Vatankhah, J. Lessard, M. P. Soriaga, Y. S. Park, *Electrochim. Acta* **2004**, *49*, 1451–1459.

[72] A. J. Bard, L. R. Faulkner, *Electrochemical Methods: Fundamentals and Application*, Wiley, New York, **2001**.

[73] M. Solsona, J. C. Vollenbroek, C. B. M. Tregouet, A. E. Nieuwelink, W. Olthuis, A. Van Den Berg, B. M. Weckhuysen, M. Odijk, *Lab Chip* **2019**, *19*, 3575–3601.

[74] B. Weinhausen, S. Köster, *Lab Chip* **2013**, *13*, 212–215.

[75] H. Y. N. Holman, R. Miles, Z. Hao, E. Wozei, L. M. Anderson, H. Yang, *Anal. Chem.* **2009**, *81*, 8564–8570.

[76] G. Kwon, Y. H. Cho, K. B. Kim, J. D. Emery, I. S. Kim, X. Zhang, A. B. F. Martinson, D. M. Tiede, *J. Synchrotron Radiat.* **2019**, *26*, 1600–1611.

[77] I. T. Neckel, L. F. Castro, F. Callefo, D. Galante, A. L. Gobbi, R. S. ; Lima, M. H. O. Piazzetta, *Dispositivo Microfluídico Selado Com Película de Poliéster.*, **2020**, BR1020200200402 30/09/2020.

[78] C. Wei, R. R. Rao, J. Peng, B. Huang, I. E. L. Stephens, M. Risch, Z. J. Xu, Y. Shao-Horn, *Adv. Mater.* **2019**, *31*, 1–24.

[79] R. Barlag, F. Nyasulu, R. Starr, J. Silverman, P. Arthasery, L. McMills, *J. Chem. Educ.* **2014**, *91*, 766–768.

[80] M. C. O. Monteiro, M. T. M. Koper, *Electrochim. Acta* **2019**, *325*, 134915.

[81] J. Clavilier, R. Faure, G. Guinet, R. Durand, *J. Electroanal. Chem.* **1980**, *107*, 205–209.

[82] Z. Borkowska, U. Slimming, *J. Electroanal. Chem.* **1991**, *312*, 237–244.

[83] A. K. Freund, *Structure* **1996**, *4*, 121–125.

[84] T. U. Schulli, S. J. Leake, *Curr. Opin. Solid State Mater. Sci.* **2018**, *22*, 188–201.

[85] C. Atlan, C. Chatelier, M. Dupraz, I. Martens, A. Viola, N. Li, L. Gao, S. J. Leake, T. U. Schülli, J. Eymery, F. Maillard, M.-I. Richard, **2022**, 1–18.

[86] L. Sun, Y. Fang, Z. Li, W. Wang, H. Chen, *Nano Res.* **2017**, *10*, 1740–1748.

[87] F. T. Patrice, K. Qiu, Y. L. Ying, Y. T. Long, *Annu. Rev. Anal. Chem.* **2019**, *12*, 347–370.

[88] L. A. Baker, *J. Am. Chem. Soc.* **2018**, DOI 10.1021/jacs.8b09747.

[89] S. Mathuri, Y. Zhu, M. M. Margoni, X. Li, *Front. Chem.* **2021**, *9*, 1–9.

[90] O. J. Wahab, M. Kang, P. R. Unwin, *Curr. Opin. Electrochem.* **2020**, *22*, 120–128.

[91] J. B. Sambur, P. Chen, *Annu. Rev. Phys. Chem.* **2014**, *65*, 395–422.

[92] M. V. Mirkin, T. Sun, Y. Yu, M. Zhou, *Acc. Chem. Res.* **2016**, *49*, 2328–2335.

[93] V. Favre-Nicolin, G. Girard, S. Leake, J. Carnis, Y. Chushkin, J. Kieffer, P. Paleo, M. I. Richard, *J. Appl. Crystallogr.* **2020**, *53*, 1404–1413.

[94] J. Xiao, S. Liu, N. Tian, Z. Y. Zhou, H. X. Liu, B. Bin Xu, S. G. Sun, *J. Am. Chem. Soc.* **2013**, *135*, 18754–18757.

[95] A. Björling, L. A. B. Marcal, R. M. Arán-Ais, J. Solla-Gullón, *ChemRXiv* **2023**, 1–27.

[96] A. Björling, L. A. B. Marçal, J. Solla-Gullón, J. Wallentin, D. Carbone, F. R. N. C. Maia, *Phys. Rev. Lett.* **2020**, *125*, 1–6.

[97] M. I. Richard, S. Labat, M. Dupraz, N. Li, E. Bellec, P. Boesecke, H. Djazouli, J. Eymery, O. Thomas, T. U. Schulli, M. K. Santala, S. J. Leake, *J. Appl. Crystallogr.* **2022**, *55*, 621–625.

[98] J. Masa, C. Andronescu, W. Schuhmann, *Angew. Chemie - Int. Ed.* **2020**, *59*, 15298–15312.

[99] A. S. Bandarenka, E. Ventosa, A. Maljusch, J. Masa, W. Schuhmann, *Analyst* **2014**, *139*, 1274–1291.

[100] M. B. C. De Souza, R. A. Vicente, V. Y. Yukuhiro, C. T. G. Pires, W. Cheuquepán, J. L. Bott-Neto, J. Solla-Gullón, P. S. Fernández, *ACS Catal.* **2019**, *9*, 5104–5110.

[101] N. Han, P. Ding, L. He, Y. Li, Y. Li, *Adv. Energy Mater.* **2020**, *10*, 1–19.

[102] C. He, Z. Y. Wu, L. Zhao, M. Ming, Y. Zhang, Y. Yi, J. S. Hu, *ACS Catal.* **2019**, *9*, 7311–7317.

[103] K. H. Saeed, M. Forster, J. F. Li, L. J. Hardwick, A. J. Cowan, *Chem. Commun.* **2020**, *56*, 1129–1132.

[104] H. Luo, V. Y. Yukuhiro, P. S. Fernández, J. Feng, P. Thompson, R. R. Rao, R. Cai, S. Favero, S. J. Haigh, J. R. Durrant, I. E. L.

Stephens, M.-M. Titirici, *ACS Catal.* **2022**, 14492–14506.

[105] R. N. Dürr, P. Maltoni, H. Tian, B. Jousselme, L. Hammarström, T. Edvinsson, *ACS Nano* **2021**, *15*, 13504–13515.

[106] W. Zheng, *Chemistry–Methods* **2022**, DOI 10.1002/cmtd.202200042.

[107] E. B. Tetteh, L. Banko, O. A. Krysiak, T. Löffler, B. Xiao, S. Varhade, S. Schumacher, A. Savan, C. Andronescu, A. Ludwig, W. Schuhmann, *Electrochem. Sci. Adv.* **2022**, *2*, 1–9.

[108] S. Amemiya, A. J. Bard, F. R. F. Fan, M. V. Mirkin, P. R. Unwin, *Annu. Rev. Anal. Chem.* **2008**, *1*, DOI 10.1146/annurev.anchem.1.031207.112938.

[109] J. Clausmeyer, M. Nebel, S. Grützke, Y. U. Kayran, W. Schuhmann, *Chempluschem* **2018**, *83*, 414–417.

[110] O. Klementieva, C. Sandt, I. Martinsson, M. Kansiz, G. K. Gouras, F. Borondics, *Adv. Sci.* **2020**, *7*, DOI 10.1002/advs.201903004.

[111] J. Solla-Gullón, P. Rodríguez, E. Herrero, A. Aldaz, J. M. Feliu, *Phys. Chem. Chem. Phys.* **2008**, *10*, 1359–1373.

[112] D. A. Schmidt, I. Kopf, E. Bründermann, *Laser Photonics Rev.* **2012**, *6*, 296–332.

[113] U. Johansson, U. Vogt, A. Mikkelsen, *X-Ray Nanoimaging: Instruments and Methods* **2013**, *8851*, 88510L.

[114] S. J. Leake, G. A. Chahine, H. Djazouli, T. Zhou, C. Richter, J. Hilhorst, L. Petit, M. I. Richard, C. Morawe, R. Barrett, L. Zhang, R. A. Homs-Regojo, V. Favre-Nicolin, P. Boesecke, T. U. Schülli, *J. Synchrotron Radiat.* **2019**, *26*, 571–584.

[115] R. Hettel, “The Evolution of 4th Generation Storage Ring Light Sources,” can be found under https://www.aps.anl.gov/sites/www.aps.anl.gov/files/APS-Uploads/ASD/2019-03-KJKFest/Presentations/Hettel - The Evolution of 4th Generation Storage Ring Light Sources.pdf, **2019**.

[116] A. Salian, S. Mandal, *Crit. Rev. Solid State Mater. Sci.* **2022**, *47*, 142–193.

[117] J. H. Park, H. S. Ahn, *Appl. Surf. Sci.* **2020**, *504*, 144517.

[118] H. Lu, J. Tournet, K. Dastafkan, Y. Liu, Y. H. Ng, S. K. Karuturi, C. Zhao, Z. Yin, *Chem. Rev.* **2021**, *121*, 10271–10366.

[119] N. Kumar Katiyar, K. Biswas, J.-W. Yeh, S. Sharma, C. Sekhar Tiwary, *Nano Energy* **2021**, *88*, 106261.

[120] T. Löffler, A. Ludwig, J. Rossmeisl, W. Schuhmann, *Angew. Chemie - Int. Ed.* **2021**, *60*, 26894–26903.